

Statistical characterization of valley coupling in Si/SiGe quantum dots via g -factor measurements near a valley vortex

Benjamin D. Woods,¹ Merritt P. Losert,¹ Nasir R. Elston,¹ M. A. Eriksson,¹ S. N. Coppersmith,² Robert Joynt,¹ and Mark Friesen¹

¹*Department of Physics, University of Wisconsin-Madison, Madison, WI 53706, USA*

²*School of Physics, University of New South Wales, Sydney, New South Wales 2052, Australia*

The presence of low-energy valley excitations in Si/SiGe heterostructures often causes spin qubits to fail. It is therefore important to develop robust protocols for characterizing the valley coupling. Here, we show that realistically sized samplings of valley energy distributions tend to dramatically overestimate the average valley coupling. But we find that knowledge of the valley phase, in addition to the valley splitting, can significantly improve our estimates. Motivated by this understanding, we propose a novel method to probe the valley phase landscape across the quantum well using simple g -factor measurements. An important calibration step in this procedure is to measure g in a loop enclosing a valley vortex, where the valley phase winds by $\pm 2\pi$ around a zero of the valley splitting. This proposal establishes an important new tool for probing spin qubits, and it can be implemented in current experiments.

Spin qubits in Si/SiGe quantum dots have made tremendous progress towards quantum computing at scale [1–5]. However, the valley degree of freedom arising from the conduction-band valley degeneracy of Si [6] presents a serious challenge, as small energy splittings E_v between the ground and excited valley states can cause decoherence [7–9] (e.g., accidental excitations), and can interfere with state preparation and measurement [10, 11]. Due to the unavoidable presence of alloy disorder in the SiGe regions of the heterostructure, E_v can vary widely from dot to dot [12]. Indeed, recent theoretical work [13–16] suggests that most, if not all, modern Si/SiGe quantum wells should fall into the “disorder-dominated” regime, in which a significant fraction of dots are guaranteed to have low E_v . While this issue may be sidestepped in experiments involving just a handful of dots, a large-scale quantum computer will unavoidably suffer from compromised or failed qubits. An important goal is therefore to engineer Si/SiGe quantum wells with “deterministically enhanced” valley splittings, for which the occurrences of low- E_v dots are exponentially suppressed. To establish such behavior, we need to determine the statistical parameters Δ_0 and σ_Δ that characterize the valley coupling distribution [13]. Here, $E_v = 2|\Delta|$, where the complex, inter-valley coupling $\Delta = \Delta_0 + \Delta_\delta$ can be decomposed into its deterministic (Δ_0) and random (Δ_δ) components. We note that Δ_0 is determined by the average Ge concentration profile (i.e., the virtual-crystal potential), while Δ_δ is determined by alloy disorder and follows a complex normal distribution with standard deviation σ_Δ . In a hopeful sign for future work, some recent experiments [17, 18] have reported valley splitting distributions with few or no instances of low valley splittings – a hallmark of deterministically enhanced behavior. However, at present, these conclusions cannot be reconciled with theoretical understanding.

To help clarify this situation, below we critically examine the standard method, namely maximum likelihood estimation, for characterizing valley splitting distributions. We focus particularly on the question of whether this method can reliably determine the parameters Δ_0 and σ_Δ by considering E_v measurements alone. We show that, in the disorder-dominated

regime (defined as $|\Delta_0|/\sigma_\Delta \lesssim \sqrt{\pi}/2$), valley splitting distributions can sufficiently mimic deterministically enhanced distributions such that differentiating them with realistically sized data sets is fraught with difficulty. To clarify this situation, we propose to use measurements of the valley phase ϕ_v [19], defined as $e^{i\phi_v} = \Delta/|\Delta|$, in addition to E_v . The valley phase is of interest for fundamental reasons [7, 10, 20], and it also provides a sensitive probe of interface and alloy disorder [13].

Unfortunately, ϕ_v cannot be probed directly [21, 22], so a robust measurement scheme is needed. Here, we propose to map out ϕ_v fluctuations by measuring the Landé g -factor. Such g -factor measurements are convenient and accurate when performed with qubit resonance experiments. The mapping relies upon a direct but largely unexplored relationship between ϕ_v and g , which we describe in detail below. To summarize: the variations of g across a sample are proportional to $\cos \phi_v$, thus taking extreme values whenever $\phi_v = 0$ or π , as governed by random-alloy fluctuations. To complete the mapping between g and ϕ_v , we must therefore apply a calibration step to identify the extrema of the g -factor. We propose to do this by first locating a valley vortex (VV), defined as one of the frequent points where $E_v = 0$. By moving a single-electron dot in a loop around the vortex, the valley phase winds between 0 and $\pm 2\pi$, as required. Indeed, a recent shuttling experiment has demonstrated that E_v can be mapped out over large regions of heterostructures [18]; here, we suggest using a similar technique to map out the g -factor and to perform the calibration step.

Characterizing the valley coupling distributions. – Knowledge of the valley splitting distribution allows us to predict the failure rate of qubits at scale. We first consider the Δ distribution, for which the real and imaginary components, Δ_r and Δ_i , are uncorrelated and normally distributed, having a probability density of

$$f(\Delta; |\Delta_0|, \phi_0, \sigma_\Delta) = (\pi\sigma_\Delta^2)^{-1} \times e^{-(\Delta_r - |\Delta_0| \cos \phi_0)^2 / \sigma_\Delta^2} e^{-(\Delta_i - |\Delta_0| \sin \phi_0)^2 / \sigma_\Delta^2}. \quad (1)$$

The distribution is determined by the average Ge concentra-

tion profile of the quantum well, the vertical electric field, and the lateral shape of the quantum dot, and is fully characterized by the parameters $|\Delta_0|$, ϕ_0 , and σ_Δ , where ϕ_0 is the average valley phase defined in $\Delta_0 = |\Delta_0|e^{i\phi_0}$. The deterministic valley coupling Δ_0 is mainly determined by the shape of the vertical confinement potential [13, 19], particularly its sharpest features, while its standard deviation σ_Δ is fully determined by the weighted overlap of the quantum dot wave function with Ge atoms [13]. Since $E_v = 2|\Delta|$ is much easier to measure than Δ , we also consider the distribution for E_v , which has a Rician form [13] given by

$$f(E_v; |\Delta_0|, \sigma_\Delta) = \frac{E_v}{2\sigma_\Delta^2} e^{-(E_v^2 + 4|\Delta_0|^2)/(4\sigma_\Delta^2)} I_0\left(\frac{E_v|\Delta_0|}{\sigma_\Delta^2}\right), \quad (2)$$

where $I_0(x)$ is a modified Bessel function of the first kind. Scaling E_v by σ_Δ in this expression, we see that the shape of the distribution is entirely determined by the ratio $|\Delta_0|/\sigma_\Delta$, with a crossover to deterministically enhanced behavior occurring when $|\Delta_0|/\sigma_\Delta > \sqrt{\pi}/2 \approx 0.9$. A natural strategy for characterizing $f(E_v)$ is to gather statistics on E_v , either from many dots on the same device [23, 24] or from one dot at many different locations [18, 24, 25]. We now show that this strategy works well in the deterministic regime but not the disordered regime, even in the limit of impractically large data sets. (E.g., see [26].)

In Fig. 1, we generate random samples from Eq. (2), and then attempt to reconstruct the distribution from these data. We begin by randomly sampling E_v for a statistically independent set of quantum dots, for two cases: $|\Delta_0|/\sigma_\Delta = 2$ (deterministic regime) and $|\Delta_0|/\sigma_\Delta = 0$ (disordered regime). We then divide these data into groups of 20, where each group is meant to represent a large but realistic experimental sample. For each group of 20 dots, we then use maximum likelihood to estimate the best-fit parameters for the Rician distribution, denoted as $|\hat{\Delta}_0|$ and $\hat{\sigma}_\Delta$. Results are shown in Fig. 1(a), where each data point represents a single group of 20 dots, with blue and red indicating the deterministic and disordered cases, respectively; the blue \times and red \star show the corresponding generating parameters for the two distributions. Note that different combinations of generating parameters $|\Delta_0|$ and σ_Δ can yield the same average valley splitting \bar{E}_v ; the dashed lines in Fig. 1(a) indicate three such families, which include the generating parameters for the data shown in the figure. We see that the red and blue data fall near the red and blue curves, as expected. The deterministic (blue) data also fall near their corresponding generating parameter (blue \times). However, a majority [27] of red data points fall far from their generating parameter (red \star), thus vastly overestimating $|\Delta_0|$. In fact, for realistically sized data sets, the method typically misclassifies disordered samples as deterministic. This dramatic overestimation of the deterministic valley coupling in the disordered regime also occurs when including an impractically larger number of dots per group (see [26]).

On the other hand, simultaneous measurements of E_v and ϕ_v provide a means of characterizing the valley splitting distribution more accurately. To see this, we follow the same procedure as before, generating data from a distribution, col-

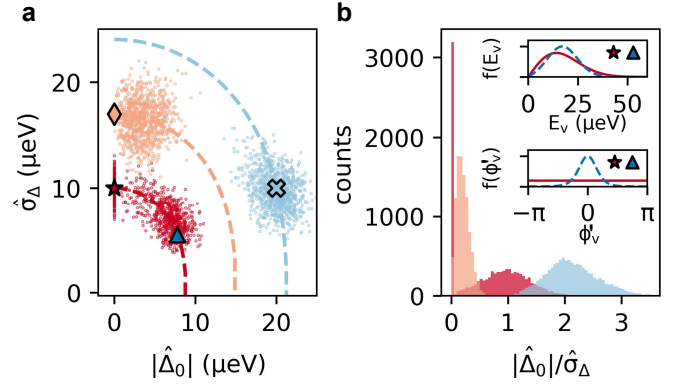


FIG. 1. Statistical characterization of valley splitting distributions. (a) Valley splittings are generated randomly from the distribution function in Eq. (2) for 10^4 groups of 20 dots. Each group of 20 is used to reconstruct the original distribution via maximum likelihood estimation, yielding the best-fit parameters $|\hat{\Delta}_0|$ and $\hat{\sigma}_\Delta$. Red and blue data show results obtained for the Rician distribution, Eq. (2), with generating parameters $(|\Delta_0|, \sigma_\Delta) = (0, 10) \mu\text{eV}$ (\star symbol) or $(20, 10) \mu\text{eV}$ (\times symbol), respectively. Salmon data show results for a complex normal distribution, Eq. (1), with generating parameters $(|\Delta_0|, \sigma_\Delta) = (0, 17) \mu\text{eV}$ and $\phi_0 = \text{arbitrary}$, because $|\Delta_0| = 0$ (\diamond symbol). Dashed lines show families of generating parameters that yield the same average \bar{E}_v , including the parameters used to generate the data. (b) Distributions of the parameter ratio $|\hat{\Delta}_0|/\hat{\sigma}_\Delta$, taken from (a). Upper inset: E_v distributions for two sets of generating parameters in (a), indicated by the star and triangle (Δ), having the same average \bar{E}_v ; for common sample sizes, these distributions are difficult to distinguish. Lower inset: $\phi'_v = \phi_v - \phi_0$ distributions for the same sets of generating parameters; here, these two distributions are easy to distinguish, which explains why valley splitting distributions are easier to characterize when ϕ_v information is available. Note that the red distribution incorrectly indicates deterministic behavior, with the majority of points showing $|\hat{\Delta}_0|/\hat{\sigma}_\Delta > \sqrt{\pi}/2$. When only E_v data are available, the distributions can be characterized accurately in the deterministic regime (blue data), but not the disordered regime (red data). When ϕ_v data are also available, the distributions can be characterized more accurately (salmon data).

lecting the data into groups of 20, and using maximum likelihood to reconstruct the original distribution. However, we now use the Δ distribution from Eq. (1), rather than the E_v distribution from Eq. (2). The results are shown as salmon data points in Fig. 1, again for the case of $|\Delta_0|/\sigma_\Delta = 0$ [28]; for visual clarity here, we use a different σ_Δ value than the red data. We see that the second method does a much better job of estimating $|\Delta_0|$ and σ_Δ than before, when only E_v data was used. Indeed, for the results shown here, no data are misclassified as deterministic.

The reason for the improved inferential power that comes from knowledge of ϕ_v is illustrated in the insets of Fig. 1(b). The top inset shows two E_v distributions having the same average E_v , but very different generating parameters $|\Delta_0|$ and σ_Δ , corresponding to the red star and blue triangle in Fig. 1(a). Despite their differences, the distributions have strikingly similar shapes, rendering them nearly indistinguishable. In contrast, the second inset shows $\phi'_v = \phi_v - \phi_0$ distributions for the same generating parameters, which are easy to distinguish.

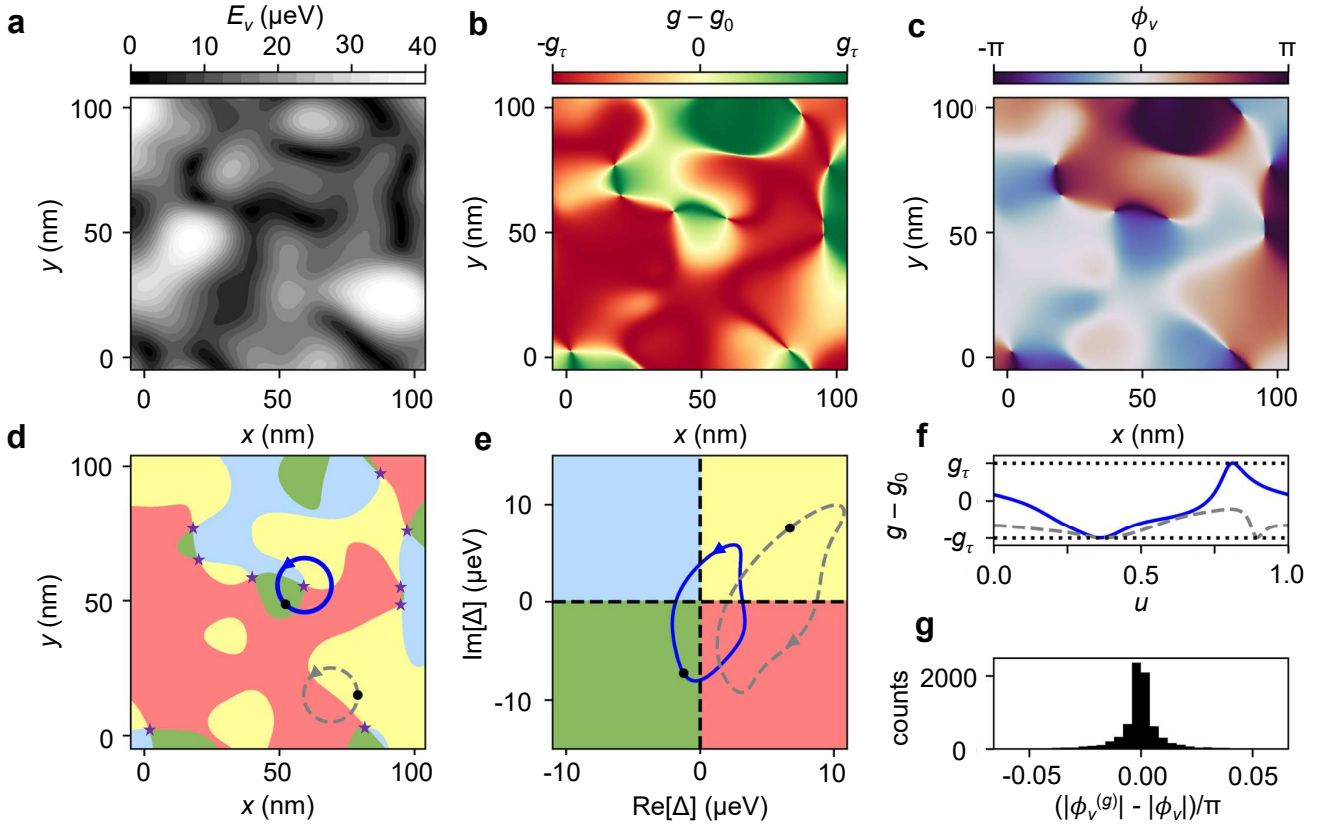


FIG. 2. Probing the valley phase using g -factor measurements. (a)–(c) Three two-dimensional landscapes are computed for a Si/SiGe dot of radius $\ell = \sqrt{\hbar/(m_t\omega_t)} = 14.2$ nm, for the same alloy disorder realization, with valley coupling parameters $(\Delta_0, \sigma_\Delta) = (0, 20)$ μeV. (a) Valley splitting (E_v) landscape. (b) g -factor landscape. (c) Valley phase (ϕ_v) landscape. Here, E_v and g are experimentally measurable, while ϕ_v can be determined from g -factor data by inverting Eq. (4). (d) The valley phase in (c) is replotted in a four-color scale, with different colors representing different quadrants of the complex Δ plane. Valley vortices (VVs) occur at points where the four colors meet (purple stars), corresponding to points where $E_v = 0$. [Compare with (a).] We propose to determine the maximum deviations of g from its average value g_0 , and thus determine the value of g_τ in Eq. (4), by measuring g around a loop containing a VV. (e) The same two paths shown in (d), plotted on the complex Δ plane. (f) Fluctuations of the g -factor, $g - g_0$, along the same two paths, as a function of a relative position variable u . Since the solid blue loop encloses one VV, $g - g_0$ is guaranteed to visit its maximum and minimum values ($\pm g_\tau$) along this path. (g) A statistical distribution of valley-phase estimation errors $|\phi_v^{(g)}| - |\phi_v|$, for 5,000 disorder realizations, where ϕ_v is the actual valley phase obtained for a ground-state wavefunction and $\phi_v^{(g)}$ is the approximate valley phase obtained by inverting Eq. (4) while ignoring the effects of random alloy disorder in g_τ . The resulting errors are very small, with a standard deviation of 0.012π .

(See [26] for a derivation of the ϕ_v distribution.)

Probing the valley phase with g -factor measurements. –

Although ϕ_v cannot be probed directly, there is a direct relation between ϕ_v and the fluctuations of g about its mean value g_0 , which can be measured accurately in qubit experiments. We now review this relationship, which was first derived in [29], and is also summarized in [26].

An effective Hamiltonian can be derived from an effective-mass model by first evaluating matrix elements in a basis labeled with spin, valley, and orbital quantum numbers, followed by projecting onto the lowest-energy orbital within a second-order Schrieffer-Wolff transformation [29]. This results in a 4×4 effective Hamiltonian given by

$$H_{\text{eff}} = \Delta\tau_- + \Delta^*\tau_+ + \frac{\mu_B g_0}{2} \mathbf{B} \cdot \boldsymbol{\sigma} + \frac{\mu_B}{2} (g_\tau\tau_- + g_\tau^*\tau_+) (B_x\sigma_y + B_y\sigma_x). \quad (3)$$

Here, $\boldsymbol{\sigma}$ is a vector of Pauli matrices in spin space and $\tau_\pm = |\pm z\rangle\langle \mp z|$ are raising/lowering operators for the $\pm z$ valley states in the conduction band of Si. The matrix elements Δ and g_τ describe spin-conserving and spin-nonconserving valley couplings, respectively, including perturbative corrections from orbitally excited states up to second order. The Zeeman term describes an in-plane magnetic field \mathbf{B} , where μ_B is the Bohr magneton and $g_0 \approx 2$ is the bare Landé g -factor. Note that $g_\tau \ll g_0$, and we may assume that $g_\tau \in \mathbb{R}_+$ without loss of generality [30]. We stress that the effective-mass model used as the starting point in deriving the effective Hamiltonian yields spin-orbit coefficients, g -factors, and valley splittings that are all in good agreement with accurate $sp^3d^5s^*$ tight-binding models [13, 31], and hence we expect the effective Hamiltonian in Eq. (3) to capture all of the relevant physics.

To compute the g -factor, we diagonalize the Δ terms of Eq. (3) in the limit $B \rightarrow 0$ and project onto the valley

ground state. We diagonalize the resulting two-dimensional spin Hamiltonian to obtain the ground and excited energies E_0 and E_1 . Defining $g = (E_1 - E_0)/(\mu_B B)$ when $B \rightarrow 0$, we obtain

$$g = g_0 - g_\tau \cos \phi_v \sin(2\theta_B), \quad (4)$$

where θ_B is the angle of \mathbf{B} with respect to the [100] crystallographic axis, i.e. $\mathbf{B} = B(\cos \theta_B \hat{x} + \sin \theta_B \hat{y})$. For experimental protocols, we may choose $\theta_B = \pi/4$ (i.e. \mathbf{B} along the [110] crystallographic axis) to maximize the size of g -factor fluctuations.

In Eqs. (3) and (4), we note that the amplitude and phase of the valley coupling vary in the plane of the quantum well due to alloy disorder, $\Delta = \Delta(x, y)$, yielding valley splitting landscapes like the one shown in Fig. 2(a), where (x, y) denotes the center of a quantum dot. The dependence of g on ϕ_v then gives rise to g -factor landscapes like the one shown in Fig. 2(b). See Ref. [29] for a description of the method used for generating E_v and ϕ_v landscapes. The central idea of this work is to invert Eq. (4) to extract ϕ_v , as shown in Fig. 2(c), through measurements of g . There are two potential challenges for implementing this procedure, which we now address.

Using valley vortices to determine g_τ . – The first challenge with inverting Eq. (4) is that g_τ is not known, a priori. An inefficient solution would be to map out g over a region large enough to include its extreme values with high probability. As a more efficient alternative, we propose to determine g_τ with certainty by measuring g around a loop enclosing a single valley vortex (VV), which we define as a point where the valley splitting vanishes: $E_v = 2|\Delta| = 0$. VVs can be seen in valley-splitting landscapes, like the one shown in Fig. 2(a); however, they are easier to visualize in a map like Fig. 2(d), where the four colors denote the four quadrants of the complex plane of Δ values; here, the VVs occur at points where the four colors meet. In Fig. 2(d), there are ten such VVs, denoted by purple stars.

To illustrate our VV proposal, we consider the two loops indicated in the spatial map of Fig. 2(d). Here, the dashed-gray and solid-blue loops enclose zero or one VV, respectively. In Fig. 2(e), we show the same paths plotted in the complex Δ plane, where it is clear that they are topologically distinct, since the solid-blue loop winds around the origin once, while the dashed-gray loop does not. The presence of a non-zero winding number is key to the procedure, as it causes ϕ_v to wind by $\pm 2\pi$, ensuring that g achieves its extreme values of $g_0 \pm g_\tau$ somewhere along the path. This is illustrated in the $g - g_0$ plot shown in Fig. 2(f), where the solid-blue loop attains both extrema, while the dashed-gray loop attains only its minimum.

This scheme is efficient for finding g_τ . However, to implement it, we must first locate a VV. A brute force scan offers an obvious, but inefficient solution. As a more efficient alternative, we propose following a curve of constant g [32]. There are only two outcomes for this procedure: (1) the curve passes through a VV (since the full range of ϕ_v values are present here), or (2) it forms a closed loop without passing through a VV. The first case is often successful; however, if

not, one should try again with a new starting point, and repeat until a VV is located. We note that it should not be difficult to locate VVs in the disordered regime, since their density is fairly high. In [26], we derive this density, obtaining

$$\rho_{\text{VV}} = (0.184/\ell^2) e^{-|\Delta_0|^2/\sigma_\Delta^2}, \quad (5)$$

where $\ell = \sqrt{\hbar/(m_t \omega_t)}$ is the quantum dot radius. Indeed, for the $100 \times 100 \text{ nm}^2$ region considered in Fig. 2, Eq. (5) predicts the occurrence of 9.2 VV, on average, while 10 VV are observed here. Note that the VV density scales with dot size, such that any dot should find the same number of VV in its vicinity (on average), regardless of its size.

Higher-order fluctuations in g . – The second challenge with inverting Eq. (4) is that it neglects higher-order effects of alloy disorder. For example, in Eq. (3), the Δ term includes disorder directly in its random component. However, the leading corrections to the g -factor from g_τ are deterministic: they only depend on disorder at third order in the perturbation theory. Fortunately, this means that disorder effects are weak in typical scenarios, as illustrated in Fig. 2(g). Here, we calculate g for a physically realistic Si/SiGe quantum well, as described in [26]. We then compare the valley phase computed via two different methods. In the first method, we generate the valley coupling landscape for one instance of alloy disorder and directly extract the absolute value of the valley phase $|\phi_v|$ (see Eq. (S.50) of [26]). Second, we use the same alloy disorder to compute $g = (E_1 - E_0)/(\mu_B B)$ in the limit $B \rightarrow 0$ by directly solving for the eigenvalues E_0 and E_1 , as described in [26]. Note that the obtained eigenvalues contain the information from the higher-order perturbations neglected in Eq. (3). We then invert Eq. (4), using the g_τ value computed in the absence of disorder, obtaining the approximate result $|\phi_v^{(g)}|$. The difference $|\phi_v^{(g)}| - |\phi_v|$ represents the error induced by neglecting higher-order corrections from alloy disorder. A distribution of $|\phi_v^{(g)}| - |\phi_v|$ values for 5,000 different disorder realizations is shown in Fig. 2(g). The errors are seen to be small, with a standard deviation of 0.012π that represents the uncertainty of the ϕ_v extraction procedure. Further discussion of this distribution is given in [26].

Conclusion. – We have shown that sampling a distribution of E_v values, with no other information, yields very poor estimates of the valley coupling parameters $|\Delta_0|$ and σ_Δ , except in rare cases where $|\Delta_0| \gtrsim \sigma_\Delta$. However, we have also shown that this situation is greatly improved when valley phase ϕ_v information is available. Motivated by this fact, we proposed to extract ϕ_v from g -factor measurements across the quantum well. A key calibration step for this procedure involves measuring the spatial variations of g around a path enclosing a valley vortex, because this reveals the full range of g values. Since characterizing $|\Delta_0|$ and σ_Δ in Si/SiGe quantum wells is a key step for enabling spin-based quantum processors at scale, we expect the current proposal to provide an important characterization tool for near-term experiments.

Acknowledgments. – This research was sponsored in part by the Army Research Office (ARO) under Awards No. W911NF-17-1-0274, W911NF-22-1-0090, and W911NF-23-1-0110. The views, conclusions, and recommendations contained in this document are those of the authors and are not

necessarily endorsed nor should they be interpreted as representing the official policies, either expressed or implied, of the

ARO or the U.S. Government. The U.S. Government is authorized to reproduce and distribute reprints for Government purposes notwithstanding any copyright notation herein.

-
- [1] G. Burkard, T. D. Ladd, A. Pan, J. M. Nichol, and J. R. Petta, Semiconductor spin qubits, *Rev. Mod. Phys.* **95**, 025003 (2023).
- [2] X. Xue, M. Russ, N. Samkharadze, B. Undseth, A. Sammak, G. Scappucci, and L. M. K. Vandersypen, Quantum logic with spin qubits crossing the surface code threshold, *Nature* **601**, 343 (2022).
- [3] A. R. Mills, C. R. Guinn, M. J. Gullans, A. J. Sigillito, M. M. Feldman, E. Nielsen, and J. R. Petta, Two-qubit silicon quantum processor with operation fidelity exceeding 99%, *Science Advances* **8**, eabn5130 (2022).
- [4] A. Noiri, K. Takeda, T. Nakajima, T. Kobayashi, A. Sammak, G. Scappucci, and S. Tarucha, Fast universal quantum gate above the fault-tolerance threshold in silicon, *Nature* **601**, 338 (2022).
- [5] S. G. J. Philips, M. T. Mądzik, S. V. Amitonov, S. L. de Snoo, M. Russ, N. Kalhor, C. Volk, W. I. L. Lawrie, D. Brousse, L. Trypuzen, B. P. Wuetz, A. Sammak, M. Veldhorst, G. Scappucci, and L. M. K. Vandersypen, Universal control of a six-qubit quantum processor in silicon, *Nature* **609**, 919 (2022).
- [6] F. A. Zwanenburg, A. S. Dzurak, A. Morello, M. Y. Simmons, L. C. L. Hollenberg, G. Klimeck, S. Rogge, S. N. Coppersmith, and M. A. Eriksson, Silicon quantum electronics, *Rev. Mod. Phys.* **85**, 961 (2013).
- [7] D. Buterakos and S. Das Sarma, Spin-valley qubit dynamics in exchange-coupled silicon quantum dots, *PRX Quantum* **2**, 040358 (2021).
- [8] J. D. Teske, F. Butt, P. Cerfontaine, G. Burkard, and H. Bluhm, Flopping-mode electron dipole spin resonance in the strong-driving regime, *Phys. Rev. B* **107**, 035302 (2023).
- [9] V. Langrock, J. A. Krzywda, N. Focke, I. Seidler, L. R. Schreiber, and L. Cywiński, Blueprint of a scalable spin qubit shuttle device for coherent mid-range qubit transfer in disordered Si/SiGe/SiO₂, *PRX Quantum* **4**, 020305 (2023).
- [10] M. L. V. Tagliaferri, P. L. Bavdaz, W. Huang, A. S. Dzurak, D. Culcer, and M. Veldhorst, Impact of valley phase and splitting on readout of silicon spin qubits, *Phys. Rev. B* **97**, 245412 (2018).
- [11] A. J. Weinstein, M. D. Reed, A. M. Jones, R. W. Andrews, D. Barnes, J. Z. Blumoff, L. E. Euliss, K. Eng, B. H. Fong, S. D. Ha, D. R. Hulbert, C. A. C. Jackson, M. Jura, T. E. Keating, J. Kerckhoff, A. A. Kiselev, J. Matten, G. Sabbir, A. Smith, J. Wright, M. T. Rakher, T. D. Ladd, and M. G. Borselli, Universal logic with encoded spin qubits in silicon, *Nature* **615**, 817 (2023).
- [12] B. P. Wuetz, M. P. Losert, S. Koelling, L. E. A. Stehouwer, A.-M. J. Zwerver, S. G. J. Philips, M. T. Mądzik, X. Xue, G. Zheng, M. Lodari, S. V. Amitonov, N. Samkharadze, A. Sammak, L. M. K. Vandersypen, R. Rahman, S. N. Coppersmith, O. Moutanabbir, M. Friesen, and G. Scappucci, Atomic fluctuations lifting the energy degeneracy in Si/SiGe quantum dots, *Nature Communications* **13**, 7730 (2022).
- [13] M. P. Losert, M. A. Eriksson, R. Joynt, R. Rahman, G. Scappucci, S. N. Coppersmith, and M. Friesen, Practical strategies for enhancing the valley splitting in Si/SiGe quantum wells, *Phys. Rev. B* **108**, 125405 (2023).
- [14] J. R. F. Lima and G. Burkard, Valley splitting depending on the size and location of a silicon quantum dot, *Phys. Rev. Mater.* **8**, 036202 (2024).
- [15] J. R. F. Lima and G. Burkard, Interface and electromagnetic effects in the valley splitting of Si quantum dots, *Materials for Quantum Technology* **3**, 025004 (2023).
- [16] L. F. Peña, J. C. Koepke, J. H. Dycus, A. Mounce, A. D. Baczewski, N. T. Jacobson, and E. Bussmann, Modeling Si/SiGe quantum dot variability induced by interface disorder reconstructed from multiperspective microscopy, *npj Quantum Inf* **10**, 33 (2024).
- [17] D. D. Esposti, L. E. A. Stehouwer, Önder Gül, N. Samkharadze, C. Déprez, M. Meyer, I. N. Meijer, L. Trypuzen, S. Karwal, M. Botifoll, J. Arbiol, S. V. Amitonov, L. M. K. Vandersypen, A. Sammak, M. Veldhorst, and G. Scappucci, Low disorder and high valley splitting in silicon, *npj Quantum Information* **10**, 32 (2024).
- [18] M. Volmer, T. Struck, A. Sala, B. Chen, M. Oberländer, T. Offermann, R. Xue, L. Visser, J.-S. Tu, S. Trellenkamp, Łukasz Cywiński, H. Bluhm, and L. R. Schreiber, Mapping of valley-splitting by conveyor-mode spin-coherent electron shuttling, *arXiv:2312.17694* (2023).
- [19] M. Friesen, S. Chutia, C. Tahan, and S. N. Coppersmith, Valley splitting theory of SiGe/Si/SiGe quantum wells, *Phys. Rev. B* **75**, 115318 (2007).
- [20] B. Tariq and X. Hu, Impact of the valley orbit coupling on exchange gate for spin qubits in silicon, *npj Quantum Information* **8**, 53 (2022).
- [21] X. Zhao and X. Hu, Measurement of tunnel coupling in a Si double quantum dot based on charge sensing, *Phys. Rev. Appl.* **17**, 064043 (2022).
- [22] F. Borjans, X. Zhang, X. Mi, G. Cheng, N. Yao, C. Jackson, L. Edge, and J. Petta, Probing the variation of the intervalley tunnel coupling in a silicon triple quantum dot, *PRX Quantum* **2**, 020309 (2021).
- [23] E. H. Chen, K. Raach, A. Pan, A. A. Kiselev, E. Acuna, J. Z. Blumoff, T. Brecht, M. D. Choi, W. Ha, D. R. Hulbert, M. P. Jura, T. E. Keating, R. Noah, B. Sun, B. J. Thomas, M. G. Borselli, C. Jackson, M. T. Rakher, and R. S. Ross, Detuning axis pulsed spectroscopy of valley-orbital states in Si/Si-Ge Quantum Dots, *Phys. Rev. Appl.* **15**, 044033 (2021).
- [24] J. C. Marcks, E. Eagen, E. C. Brann, M. P. Losert, T. Oh, J. Reily, C. S. Wang, D. Keith, F. A. Mohiyaddin, F. Luthi, M. J. Curry, J. Zhang, F. J. Heremans, M. Friesen, and M. A. Eriksson, Valley splitting correlations across a silicon quantum well, *arXiv:2504.12455* (2025).
- [25] T. Struck, M. Volmer, L. Visser, T. Offermann, R. Xue, J.-S. Tu, S. Trellenkamp, Łukasz Cywiński, H. Bluhm, and L. R. Schreiber, Spin-EPR-pair separation by conveyor-mode single electron shuttling in Si/SiGe, *Nature Communications* **15**, 1325 (2024).
- [26] See Supplementary Materials for additional technical details and statistical results.
- [27] We also observe an enhancement of counts with $|\hat{\Delta}_0| = 0$, caused by $|\hat{\Delta}_0| = 0$ being an endpoint of the fitting procedure.
- [28] Note that there is no enhancement of counts at $|\hat{\Delta}_0| = 0$ in this case, because this is no longer an endpoint in the fitting

procedure.

- [29] B. D. Woods, M. P. Losert, R. Joynt, and M. Friesen, *g*-factor theory of Si/SiGe quantum dots: spin-valley and giant renormalization effects, [arXiv:2412.19795 \(2025\)](#).
- [30] More generally, $g_\tau \in \mathbb{C}$; however, the zero of the valley phase can be redefined to give $g_\tau \in \mathbb{R}_+$, without loss of generality.
- [31] B. D. Woods, M. A. Eriksson, R. Joynt, and M. Friesen, Spin-orbit enhancement in Si/SiGe heterostructures with oscillating Ge concentration, [Phys. Rev. B **107**, 035418 \(2023\)](#).
- [32] In Fig. 2(b), such curves are obtained by starting at a random point and following a path that remains at the same color as the starting point.

Supplementary Materials: Statistical characterization of valley coupling in Si/SiGe quantum dots via g -factor measurements near a valley vortex

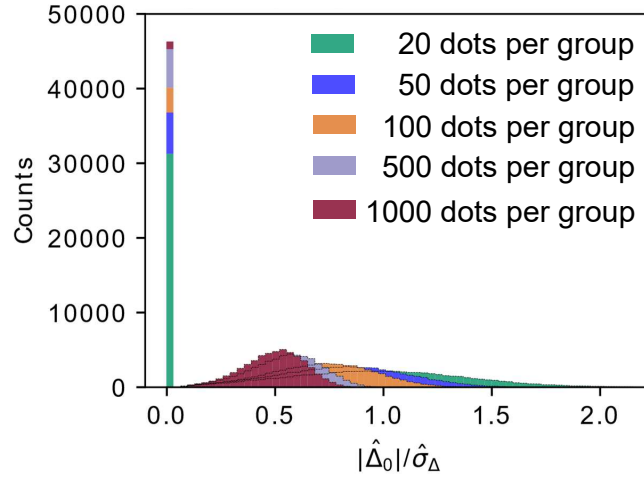


FIG. S.1. Histogram of the distribution of best-fit estimates for the ratio $|\hat{\Delta}_0|/\hat{\sigma}_\Delta$, obtained for 100,000 groups of dots with generating parameters $(|\Delta_0|, \sigma_\Delta) = (0, 10) \mu\text{eV}$. The five colors (green, blue, orange, purple, red) correspond to different numbers N of dots in the group, with $N = 20, 50, 100, 500$, and 1000 . Note that $N = 20$ was used for the results in Fig. 1 of the main text. We see that even for the case of $N = 1000$ dots per group, which is well beyond the size of modern quantum dot arrays, a significant, non-zero deterministic component $|\hat{\Delta}_0|$ is inferred in over half of the cases. Note that the ordering of histograms are inverted for the bin near $|\hat{\Delta}_0|/\hat{\sigma}_\Delta = 0$ such that the data for each N is visible.

S.1. CHARACTERIZING THE VALLEY SPLITTING DISTRIBUTION WITH A LARGER NUMBER OF DOTS

In Fig. 1 of the main text, for the red and blue data, we performed maximum likelihood estimation using groups of $N = 20$ dots to determine the best-fit parameters $|\hat{\Delta}_0|$ and $\hat{\sigma}_\Delta$ describing those valley splitting distributions. From those results, we concluded that $|\Delta_0|$ and σ_Δ can be determined with reasonable accuracy from E_v data alone, if they are in the deterministically enhanced regime, but not when they are in the disordered regime. In this Supplementary Materials section, we show that this conclusion continues to hold true, even when an impractically large number of dots are included in the analysis. To do so, we perform the same maximum likelihood estimation analysis as the main text, with generating parameters $(|\Delta_0|, \sigma_\Delta) = (0, 10) \mu\text{eV}$ corresponding to the completely disordered regime. Here, however, we vary the number of dots N in each group. The resulting best-fit ratios $|\hat{\Delta}_0|/\hat{\sigma}_\Delta$ are shown in Fig. S.1 for 100,000 groups of size $N = 20$ (green), 50 (blue), 100 (orange), 500 (purple), and 1000 (red) dots. We obtain results for $N = 20$ that are in agreement with the red data of Fig. 1 of the main text, as expected. For larger group sizes, the best-fit results slowly approach the correct answer ($|\Delta_0|/\sigma_\Delta = 0$). However, even in the case of $N = 1000$ dots per group, which is well beyond the size of state-of-the-art quantum dot arrays, a ratio $|\hat{\Delta}_0|/\hat{\sigma}_\Delta$ significantly greater than 0 is incorrectly inferred in over half of the cases.

S.2. DISTRIBUTION OF COMPLEX INTER-VALLEY COUPLING Δ

To obtain the salmon-color data set in Fig. 1 of the main text, we randomly sample Δ in groups of 20 dots and perform maximum likelihood estimation of the best-fit parameters $|\hat{\Delta}_0|$ and $\hat{\sigma}_\Delta$. In this Supplementary Materials section, we provide details regarding the complex distribution of Δ .

Recall that we can decompose the inter-valley coupling as $\Delta = \Delta_0 + \Delta_\delta$, where Δ_0 and Δ_δ are the deterministic and random components, respectively. Here, $\Delta_0 = |\Delta_0|e^{i\phi_0}$. The random component Δ_δ follows a complex Gaussian distribution with uncorrelated real and imaginary components, both having a variance of $\sigma_\Delta^2/2$ and zero mean [13]. It follows that the real (Δ_r)

and imaginary (Δ_i) components of Δ both have normal distributions given by

$$f(\Delta_r; |\Delta_0|, \phi_0, \sigma_\Delta) = \frac{1}{\sqrt{\pi\sigma_\Delta^2}} e^{-(\Delta_r - |\Delta_0| \cos \phi_0)^2 / \sigma_\Delta^2}, \quad (\text{S.1})$$

$$f(\Delta_i; |\Delta_0|, \phi_0, \sigma_\Delta) = \frac{1}{\sqrt{\pi\sigma_\Delta^2}} e^{-(\Delta_i - |\Delta_0| \sin \phi_0)^2 / \sigma_\Delta^2}. \quad (\text{S.2})$$

These distributions are both characterized by the variables $|\Delta_0|$, ϕ_0 , and σ_Δ . Our maximum likelihood estimation therefore also includes a best-fit parameter $\hat{\phi}_0$, in addition to the best-fit parameters $|\hat{\Delta}_0|$ and $\hat{\sigma}_\Delta$ use for the E_v distribution. ϕ_0 has no impact on the valley splitting E_v distribution, however, so we do not report it in Fig. 1 of the main text. Moreover, one can always remove a non-zero ϕ_0 by a global redefinition of the valley degrees of freedom.

S.3. VALLEY PHASE PROBABILITY DISTRIBUTION DERIVATION

In Fig. 1 of the main text, we plot the distribution of the relative valley phase $\phi'_v = \phi_v - \phi_0$, where $\Delta_0 = |\Delta_0|e^{i\phi_0}$. In this Supplementary Materials section, we derive this distribution.

We first define a “rotated” inter-valley coupling $\Delta' = \Delta e^{-i\phi_0} = |\Delta|e^{i\phi'_v}$, such that the rotated deterministic component is real and nonnegative, $\Delta'_0 = |\Delta_0|$. The distribution functions of the real and imaginary components of Δ' are then given by

$$f(\Delta'_r; |\Delta_0|, \sigma_\Delta) = \frac{1}{\sqrt{\pi\sigma_\Delta^2}} e^{-((\Delta'_r - |\Delta_0|)^2) / \sigma_\Delta^2}, \quad (\text{S.3})$$

$$f(\Delta'_i; \sigma_\Delta) = \frac{1}{\sqrt{\pi\sigma_\Delta^2}} e^{-(\Delta'_i)^2 / \sigma_\Delta^2}. \quad (\text{S.4})$$

We further define ϕ'_v to be in the interval $(-\pi, \pi]$. The cumulative distribution function of ϕ'_v is then given by

$$F(\phi'_v; |\Delta_0|, \sigma_\Delta) = \int_{-\infty}^{\infty} \int_{-\infty}^{\infty} f(\Delta'_r; |\Delta_0|, \sigma_\Delta) f(\Delta'_i; \sigma_\Delta) \Theta(\phi'_v - \text{Arg}(\Delta'_r + i\Delta'_i)) d\Delta'_r d\Delta'_i, \quad (\text{S.5})$$

where $\Theta(x)$ is the Heaviside step function, and $\text{Arg}(x)$ is the argument function restricted to its principle value in the interval $(-\pi, \pi]$. The integral in Eq. (S.5) is easier to handle in polar coordinates, where we find

$$F(\phi'_v; |\Delta_0|, \sigma_\Delta) = \frac{1}{\pi\sigma_\Delta^2} e^{-|\Delta_0|^2 / \sigma_\Delta^2} \int_{-\pi}^{\pi} \int_0^{\infty} e^{\frac{-r^2 + 2|\Delta_0|r \cos \phi}{\sigma_\Delta^2}} \Theta(\phi'_v - \phi) r dr d\phi \quad (\text{S.6})$$

$$= \frac{1}{\pi\sigma_\Delta^2} e^{-|\Delta_0|^2 / \sigma_\Delta^2} \int_{-\pi}^{\phi'_v} \int_0^{\infty} e^{\frac{-r^2 + 2|\Delta_0|r \cos \phi}{\sigma_\Delta^2}} r dr d\phi. \quad (\text{S.7})$$

The corresponding probability density function, plotted in the lower inset of Fig. 1 in the main text, is then given by

$$f(\phi'_v; |\Delta_0|, \sigma_\Delta) = \frac{\partial F(\phi'_v)}{\partial \phi'_v} = \frac{1}{\pi\sigma_\Delta^2} e^{-|\Delta_0|^2 / \sigma_\Delta^2} \int_0^{\infty} e^{\frac{-r^2 + 2|\Delta_0|r \cos \phi'_v}{\sigma_\Delta^2}} r dr \quad (\text{S.8})$$

$$= \frac{1}{2\pi} e^{-|\Delta_0|^2 / \sigma_\Delta^2} + \frac{|\Delta_0| \cos \phi'_v}{2\sqrt{\pi}\sigma_\Delta} e^{-|\Delta_0|^2 \sin^2 \phi'_v / \sigma_\Delta^2} \left[1 + \text{erf} \left(\frac{|\Delta_0| \cos \phi'_v}{\sigma_\Delta} \right) \right], \quad (\text{S.9})$$

where $\text{erf}(x)$ is the error function. In terms of the original valley phase variable $\phi_v = \phi'_v + \phi_0$, the distribution function is given by

$$f(\phi_v; |\Delta_0|, \sigma_\Delta) = \frac{1}{2\pi} e^{-|\Delta_0|^2 / \sigma_\Delta^2} + \frac{|\Delta_0| \cos(\phi_v - \phi_0)}{2\sqrt{\pi}\sigma_\Delta} e^{-|\Delta_0|^2 \sin^2(\phi_v - \phi_0) / \sigma_\Delta^2} \left[1 + \text{erf} \left(\frac{|\Delta_0| \cos(\phi_v - \phi_0)}{\sigma_\Delta} \right) \right]. \quad (\text{S.10})$$

S.4. DENSITY OF VALLEY VORTICES

In this Supplementary Materials section, we analytically determine the density ρ_{VV} of valley vortices (VVs) as a function of the parameter ratio $|\Delta_0|/\sigma_\Delta$. This quantity is of interest, because our protocol for extracting the valley phase ϕ_v relies on a

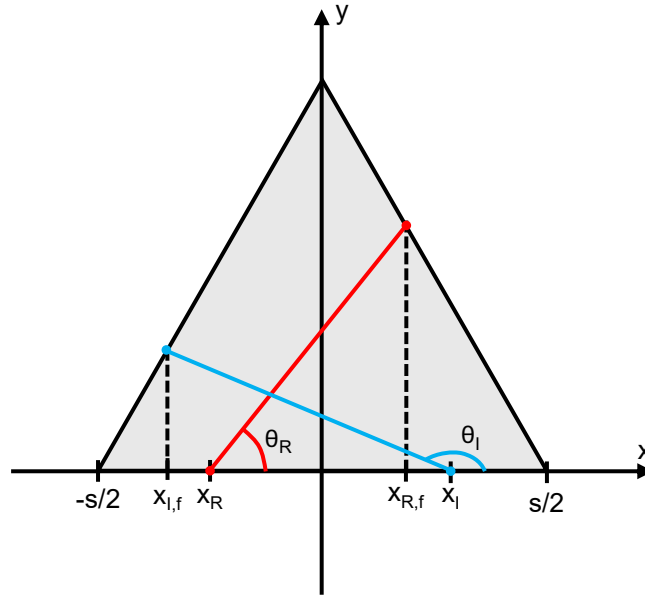


FIG. S.2. Equilateral triangle of side-length s , used to calculate the density of valley vortices. Red and blue lines correspond to $\text{Re}[\Delta] = 0$ and $\text{Im}[\Delta] = 0$, respectively. See text in sub-problem 3 for description of the parameters $\{\theta_R, \theta_I, x_R, x_I, x_{R,f}, x_{I,f}\}$.

calibration step in which the g -factor is measured in a loop enclosing a VV, so it is helpful to know their distribution: the protocol is only practical if VVs can be found within a moderately small area. Below, we show that the density is relatively high.

To begin, we again decompose the inter-valley coupling as $\Delta(x, y) = \Delta_0 + \Delta_\delta(x, y)$, where Δ_0 and Δ_δ are the deterministic and random components, respectively. Without loss of generality, we assume $\Delta_0 \in \mathbb{R}_0^+$. Let us also decompose Δ_δ into real and imaginary components, $\Delta_\delta(x, y) = R(x, y) + iI(x, y)$. The statistics of Δ depends on the spatial correlations of R and I across the quantum well. These correlations, first discussed in Ref. [13], are given by

$$\langle R(\mathbf{r}_1)R(\mathbf{r}_2) \rangle = \langle I(\mathbf{r}_1)I(\mathbf{r}_2) \rangle = \frac{\sigma_\Delta^2}{2} e^{-|\mathbf{r}_1 - \mathbf{r}_2|^2 / (2\ell_t^2)}, \quad (\text{S.11})$$

$$\langle R(\mathbf{r}_1)I(\mathbf{r}_2) \rangle = 0. \quad (\text{S.12})$$

Here, we assume a circular dot with transverse radius $\ell_t = \sqrt{\hbar / (m_t \omega_t)}$.

To determine the density of VVs, we consider an equilateral triangle of side-length s , as shown in Fig. S.2. Let us denote the probability of finding n VVs in this triangle as $P_n^\Delta(s)$. It should become less likely to observe more than one vortex inside the triangle when triangles are small; thus,

$$\lim_{s \rightarrow 0} \frac{P_n^\Delta(s)}{P_1^\Delta(s)} = 0, \quad (\text{S.13})$$

for $n \geq 2$, and the vortex density is determined by P_1^Δ , such that

$$\rho_{\text{VV}} = \lim_{s \rightarrow 0} \frac{4P_1^\Delta(s)}{\sqrt{3}s^2}, \quad (\text{S.14})$$

where $\sqrt{3}s^2/4$ is the area of the equilateral triangle. Therefore, our problem reduces to finding $P_1^\Delta(s)$ to order $\mathcal{O}(s^2)$. Note that the necessary condition for a point (x, y) to be a valley vortex is that $\text{Re}[\Delta(x, y)] = \text{Im}[\Delta(x, y)] = 0$.

To compute $P_1^\Delta(s)$, we break the problem down into three sub-problems. The first sub-problem is to determine the probability that a line segment of length s contains a point (x, y) for which $\text{Re}[\Delta(x, y)] = 0$. The second sub-problem is to determine the probability that lines defined by $\text{Re}[\Delta] = 0$ or $\text{Im}[\Delta] = 0$ cross through an equilateral triangle. This result makes use of sub-problem 1 and simple symmetry arguments. The third sub-problem is to determine the probability that lines defined by $\text{Re}[\Delta] = 0$ and $\text{Im}[\Delta] = 0$ additionally intersect within the triangle. The results of sub-problems 2 and 3 are then combined to give the final result for ρ_{VV} .

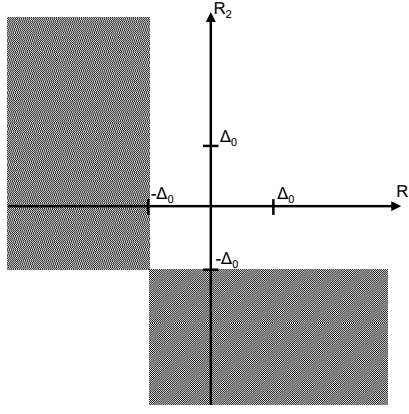


FIG. S.3. The parameter space of the real component $R(x, y)$ of the fluctuating part of the inter-valley coupling $\Delta(x, y)$, for the two points $(x, y) = \mathbf{r}_1$ and \mathbf{r}_2 . Here, $R_1 = R(\mathbf{r}_1)$ and $R_2 = R(\mathbf{r}_2)$. The hatched regions denote the parameter space regions where $\text{Re}[\Delta(\mathbf{r}_1)]$ and $\text{Re}[\Delta(\mathbf{r}_2)]$ are of opposite sign.

A. Sub-problem 1: Probability of observing $\text{Re}[\Delta] = 0$ or $\text{Im}[\Delta] = 0$ on a 1-dimensional line segment

We define $P_{\bullet\bullet}^R(s)$ as the probability that $\text{Re}[\Delta(x, y)] = \Delta_0 + R(x, y) = 0$ somewhere along a line segment of length s as $s \rightarrow 0$. In this limit, $P_{\bullet\bullet}^R(s)$ is equal to the probability that $\text{Re}[\Delta(\mathbf{r}_1)]$ and $\text{Re}[\Delta(\mathbf{r}_2)]$ are of opposite sign, where \mathbf{r}_1 and \mathbf{r}_2 are the endpoints of the line segment. Within the parameter space of $R_1 = R(\mathbf{r}_1)$ and $R_2 = R(\mathbf{r}_2)$, this condition is satisfied in the hatched regions of Fig. S.3.

The covariance properties of $\Delta(x, y)$ are known [13], with the covariance matrix of R_1 and R_2 given by

$$\Sigma = \frac{\sigma_\Delta^2}{2} \begin{pmatrix} 1 & e^{-s^2/(2\ell_t^2)} \\ e^{-s^2/(2\ell_t^2)} & 1 \end{pmatrix}. \quad (\text{S.15})$$

The corresponding joint probability density function is then given by the multi-variable normal distribution

$$f_{R_1, R_2}(R_1, R_2) = \frac{1}{2\pi\sqrt{|\Sigma|}} e^{-\frac{1}{2}\mathbf{R}^T \Sigma^{-1} \mathbf{R}}, \quad (\text{S.16})$$

where $\mathbf{R} = (R_1, R_2)^T$. $P_{\bullet\bullet}^R(s)$ is then given by the integral

$$P_{\bullet\bullet}^R(s) = 2 \int_{-\Delta_0}^{-\Delta_0} \int_{-\Delta_0}^{\infty} f_{R_1, R_2}(R_1, R_2) dR_1 dR_2 + \mathcal{O}(s^2), \quad (\text{S.17})$$

which simplifies via a change of variables:

$$R'_1 = \frac{R_1 + R_2}{\sqrt{2}}, \quad (\text{S.18})$$

$$R'_2 = \frac{-R_1 + R_2}{\sqrt{2}}. \quad (\text{S.19})$$

This diagonalizes the covariance matrix, giving

$$\Sigma' = \frac{\sigma_\Delta^2}{2} \begin{pmatrix} 1 + e^{-s^2/(2\ell_t^2)} & 0 \\ 0 & 1 - e^{-s^2/(2\ell_t^2)} \end{pmatrix} \approx \frac{\sigma_\Delta^2}{2} \begin{pmatrix} 2 & 0 \\ 0 & \frac{s^2}{2\ell_t^2} \end{pmatrix}, \quad (\text{S.20})$$

and the factorizable joint probability distribution function

$$f_{R'_1, R'_2}(R'_1, R'_2) = f_{R'_1}(R'_1) f_{R'_2}(R'_2) \approx \frac{1}{2\pi\sigma_\Delta^2} \left(\frac{2\ell_t}{s} \right) \exp\left[-\frac{(R'_1)^2}{2\sigma_\Delta^2}\right] \exp\left[-\frac{2\ell_t^2}{s^2} \frac{(R'_2)^2}{2\sigma_\Delta^2}\right]. \quad (\text{S.21})$$

The integral in Eq. (S.17) then reduces to

$$P_{\bullet\bullet}^R(s) = \frac{1}{\pi\sigma_\Delta^2} \left(\frac{2\ell_t}{s} \right) \int_0^\infty \exp\left[-\frac{2\ell_t^2}{s^2} \frac{(R'_2)^2}{2\sigma_\Delta^2}\right] \left(\int_{-\sqrt{2}\Delta_0 - R'_2}^{-\sqrt{2}\Delta_0 + R'_2} \exp\left[-\frac{(R'_1)^2}{2\sigma_\Delta^2}\right] dR'_1 \right) dR'_2 + \mathcal{O}(s^2). \quad (\text{S.22})$$

Here, the inner R'_1 integral can be written in terms of an error function involving R'_2 . Only small values of R'_2 are relevant in the limit $s \rightarrow 0$, however, because the first exponential factor in Eq. (S.22) is strongly suppressed. The inner R'_1 integral can therefore be expanded to first order in R'_2 , giving

$$\int_{-\sqrt{2}\Delta_0 - R'_2}^{-\sqrt{2}\Delta_0 + R'_2} \exp\left[-\frac{(R'_1)^2}{2\sigma_\Delta^2}\right] dR'_1 = 2R'_2 e^{-\Delta_0^2/\sigma_\Delta^2} + \mathcal{O}((R'_2)^3). \quad (\text{S.23})$$

Thus, Eq. (S.22) is given by

$$\begin{aligned} P_{\bullet\bullet}^R(s) &= \frac{4}{\pi\sigma_\Delta^2} \left(\frac{\ell_t}{s}\right) e^{-\Delta_0^2/\sigma_\Delta^2} \int_0^\infty R'_2 \exp\left[-\frac{2\ell_t^2 (R'_2)^2}{s^2 2\sigma_\Delta^2}\right] dR'_2 + \mathcal{O}(s^2) \\ &= \frac{s}{\pi\ell_t} e^{-\Delta_0^2/\sigma_\Delta^2} + \mathcal{O}(s^2), \end{aligned} \quad (\text{S.24})$$

giving the final solution to sub-problem 1.

Following similar methods, we obtain the probability $P_{\bullet\bullet}^I(s)$ of finding $\text{Im}[\Delta(x, y)] = 0$ somewhere along a line segment of length s , yielding

$$P_{\bullet\bullet}^I(s) = \frac{s}{\pi\ell_t} + \mathcal{O}(s^2) \quad (\text{S.25})$$

B. Sub-problem 2: Probability that the lines $\text{Re}[\Delta] = 0$ or $\text{Im}[\Delta] = 0$ cut through an equilateral triangle

We define $P_\Delta^R(s)$ as the probability that a line defined by $\text{Re}[\Delta] = 0$ passes through an equilateral triangle of side-length s , as $s \rightarrow 0$. In this limit, any smooth line would have to pass through two of the three edges of the triangle. Due to rotational symmetry, the probability of a $\text{Re}[\Delta] = 0$ line passing through any of the three triangle edges is the same. We therefore have

$$\begin{aligned} \lim_{s \rightarrow 0} P_\Delta^R(s) &= \frac{3}{2} \lim_{s \rightarrow 0} P_{\bullet\bullet}(s) \\ &= \frac{3s}{2\pi\ell_t} e^{-\Delta_0^2/\sigma_\Delta^2}. \end{aligned} \quad (\text{S.26})$$

Similarly, the probability $P_\Delta^I(s)$ of a line defined by $\text{Im}[\Delta] = 0$ passing through an equilateral triangle of side-length s , as $s \rightarrow 0$, is given by

$$\lim_{s \rightarrow 0} P_\Delta^I(s) = \frac{3s}{2\pi\ell_t}. \quad (\text{S.27})$$

Finally, since $R(\mathbf{r})$ and $I(\mathbf{r})$ are statistically independent, the probability $P_\Delta(s)$ of lines defined by $\text{Re}[\Delta] = 0$ and $\text{Im}[\Delta] = 0$ both passing through an equilateral triangle of side-length s is given by the simple product

$$\begin{aligned} P_\Delta(s) &= P_\Delta^R(s) P_\Delta^I(s) \\ &= \frac{9s^2}{4\pi^2\ell_t^2} e^{-\Delta_0^2/\sigma_\Delta^2} + \mathcal{O}(s^3). \end{aligned} \quad (\text{S.28})$$

C. Sub-problem 3: Probability that lines $\text{Re}[\Delta] = 0$ and $\text{Im}[\Delta] = 0$ cross inside an equilateral triangle

We define P_{int} as the probability that lines defined by $\text{Re}[\Delta] = 0$ and $\text{Im}[\Delta] = 0$ cross inside an equilateral triangle, given that both lines pass through the triangle. To compute P_{int} , we must specify the distributions from which the lines are sampled. In the limit $s \rightarrow 0$, smooth lines passing through an equilateral triangle are effectively straight line segments. The two lines pass through at least one common edge. Without loss of generality, we choose this edge to be the bottom edge of the triangle, along the x -axis, between the points $x = \pm s/2$. Figure S.2 shows an example configuration, with $\text{Re}[\Delta] = 0$ and $\text{Im}[\Delta] = 0$ illustrated as red and blue line segments, respectively. Since the dots used to compute Δ are isotropic, the orientations of the two lines (θ_R and θ_I) should have no preferred direction and should be drawn from a uniform distribution over $[0, \pi)$. Moreover, due to translational invariance, the points of intersection between the two lines and the bottom edge of the triangle, defined as x_R and x_I , are drawn from a uniform distribution between $x = \pm s/2$. The x locations where the lines exit the triangle are denoted

as $x_{R,f}$ and $x_{I,f}$ in the figure. We see that the two lines intersect if and only if $x_{R,f} - x_{I,f}$ and $x_R - x_I$ are of opposite sign. The probability of intersection is therefore given by

$$P_{\text{int}} = \frac{1}{4\pi^2 s^2} \int_{-\pi}^{\pi} \int_{-\pi}^{\pi} \int_{-s/2}^{x_I} \int_{-s/2}^{s/2} \Theta [x_{R,f}(x_R, \theta_R) - x_{I,f}(x_I, \theta_I)] dx_I dx_R d\theta_I d\theta_R \\ + \frac{1}{4\pi^2 s^2} \int_{-\pi}^{\pi} \int_{-\pi}^{\pi} \int_{x_I}^{s/2} \int_{-s/2}^{s/2} \Theta [-x_{R,f}(x_R, \theta_R) + x_{I,f}(x_I, \theta_I)] dx_I dx_R d\theta_I d\theta_R. \quad (\text{S.29})$$

Numerical evaluation of the integral yields

$$P_{\text{int}} \approx 0.349. \quad (\text{S.30})$$

D. Final result

Putting everything together, we see that the probability $P_1^\Delta(s)$ that an equilateral triangle of side-length s encloses a single VV, as $s \rightarrow 0$, is given by the probability of having the lines $\text{Re}[\Delta] = 0$ and $\text{Im}[\Delta] = 0$ both traverse the triangle, multiplied by the probability P_{int} that they also cross within the triangle:

$$\lim_{s \rightarrow 0} P_1^\Delta(s) = P_{\text{int}} \lim_{s \rightarrow 0} P_\Delta(s). \quad (\text{S.31})$$

Combining Eqs. (S.14), (S.28), (S.30), and (S.31), the density of VVs is finally given by

$$\rho_{\text{VV}} = P_{\text{int}} \frac{9}{\sqrt{3}\pi^2 \ell_t^2} e^{-\Delta_0^2/\sigma_\Delta^2} \\ \approx \frac{0.184}{\ell_t^2} e^{-\Delta_0^2/\sigma_\Delta^2}, \quad (\text{S.32})$$

which is the result given in Eq. (5) of the main text.

S.5. DETAILS OF THE DERIVATION OF THE MODEL HAMILTONIAN

In this Supplementary Materials section, we provide details regarding the calculation the effective Hamiltonian Eq. (3) in the main text. We use the same effective mass model as [29]. For clarity, we summarize some of those calculations here. We emphasize that this effective model yields spin-orbit coefficients, g -factors, and valley splittings that are good agreement with quantitatively accurate $sp^3d^5s^*$ tight-binding models [13, 31].

We consider a quantum dot in a Si/SiGe quantum well with a sigmoidal Ge concentration profile

$$n_{\text{Ge}}(z) = \frac{n_{\text{bar}}}{1 + e^{4z/W}}, \quad (\text{S.33})$$

where $n_{\text{bar}} = 0.3$ is the Ge concentration in the SiGe barrier region and $W = 0.8$ nm is the interface width measured in state-of-the-art devices [12]. We assume a vertical electric field of $F_z = 5$ mV/nm that pulls the electronic wavefunction up against the quantum well interface. [Note that a second SiGe barrier region is excluded from Eq. (S.33), as the vertical electric field is large enough that a second barrier would insignificantly affect the wavefunction, except for cases of very thin quantum wells.] In addition, we assume an isotropic in-plane harmonic, quantum-dot confinement potential with an orbital spacing of $\hbar\omega_t = 2$ meV.

The system is modeled by an effective-mass Hamiltonian with both spin and valley degrees of freedom, given by

$$H = \frac{\hbar^2}{2} \left(\frac{\hat{\pi}_z^2}{m_l} + \frac{\hat{k}_x^2 + \hat{k}_y^2}{m_t} \right) + V(\mathbf{r}) + \frac{\mu_B g_0}{2} \mathbf{B} \cdot \boldsymbol{\sigma} + \left(\left[(\mathbf{r}) e^{-i2k_0 z} + \beta_0 e^{i2k_1 z} \left(\hat{k}_x \sigma_x - \hat{k}_y \sigma_y \right) \right] \tau_- + \text{h.c.} \right), \quad (\text{S.34})$$

where $\hat{\pi}_z = \hat{k}_z + (e/\hbar)A_z(x, y)$, $\hat{k}_j = -i\partial_j$, $m_l = 0.91m_e$ and $m_t = 0.19m_e$ [6] are the longitudinal and transverse effective masses, respectively. Note that $\mathbf{A} = A_z(x, y)\hat{z}$ with $A_z(x, y) = B_x y - B_y x$ is the vector potential satisfying $\mathbf{B} = \nabla \times \mathbf{A}$. Here, σ_j are Pauli spin matrices, with $j \in \{x, y, z\}$, and $\tau_\pm = |\pm z\rangle \langle \mp z|$ is a valley raising/lowering operator with $\pm z$ denoting the two valleys near the Z point in the conduction band structure of Si. The confinement potential is given by

$$V(\mathbf{r}) = V_l(z) + \frac{m_t \omega_t^2}{2} (x^2 + y^2) + V_{\text{dis}}(\mathbf{r}), \quad (\text{S.35})$$

where V_l is the quantum well confinement potential arising from the Ge concentration profile $n_{\text{Ge}}(z)$ and the external electric field, but does not include random-alloy fluctuations, $\hbar\omega_t$ is the orbital splitting of an in-plane harmonic confinement potential representing a quantum dot, and V_{dis} describes the potential fluctuations caused by random-alloy disorder, which are discussed in more detail below. The longitudinal potential is explicitly given by

$$V_l(z) = eF_z z + E_{\text{Ge}} n_{\text{Ge}}(z), \quad (\text{S.36})$$

where $E_{\text{Ge}} = 0.6$ eV gives the desired band offset between atomic layers with different Ge concentrations. The τ_- term in Eq. (S.34) describes inter-valley coupling, where the $2k_0$ and $2k_1$ terms describe normal (i.e. spin-conserving) valley coupling and Dresselhaus spin-orbit coupling, respectively. Here, $2k_0 \approx 0.83(4\pi/a_0)$ and $2k_1 = 4\pi/a_0 - 2k_0$ correspond to wave vectors connecting valleys in the same or neighboring Brillouin zones, respectively, in the Si band structure. We emphasize that these inter-valley coupling terms yield precisely the same momentum selection rules as $sp^3d^5s^*$ tight-binding models [31]. In other words, the spin-orbit coupling terms in the effective-mass Hamiltonian are not ad-hoc, but rather, they can be related to the physics of more-detailed tight-binding models.

The Zeeman coupling, vector-potential coupling, inter-valley coupling, and alloy-disorder terms are all small compared to the kinetic energy and confinement terms in Eq. (S.34). We therefore work in the basis that diagonalizes the Hamiltonian in the absence of such perturbations. These basis states are denoted by $|\nu, n_x, n_y, \tau, \sigma\rangle$ where ν , n_x , and n_y are spatial orbital indices, and $\tau \in \{+z, -z\}$ and $\sigma \in \{\uparrow, \downarrow\}$ denote the valley and spin, respectively. The spatial wavefunctions are given by $\langle \mathbf{r} | \nu, n_x, n_y \rangle = \varphi_\nu(z) \chi_{n_x, n_y}(x, y)$, where χ_{n_x, n_y} is an in-plane harmonic-oscillator orbital with energy $\hbar\omega_t(n_x + n_y + 1)$ arising from the quantum-dot harmonic confinement potential, and φ_ν is a subband wavefunction satisfying

$$\left[\frac{\hbar^2 \hat{k}_z^2}{2m_t} + V_l(z) \right] \varphi_\nu(z) = \varepsilon_\nu \varphi_\nu(z), \quad (\text{S.37})$$

where ε_ν is the subband energy. Here, we solve for the subband wavefunctions φ_ν and energies ε_ν numerically using conventional finite-difference methods for one-dimensional differential equations.

In the new basis, the Hamiltonian is given by

$$H_{\mathbf{m}, \mathbf{n}}^{\mu, \nu} = \delta_{\mu, \nu} \delta_{\mathbf{m}, \mathbf{n}} \left[\varepsilon_{\nu, \mathbf{n}} + \frac{\mu B g_0}{2} \mathbf{B} \cdot \boldsymbol{\sigma} \right] + k_z^{\mu, \nu} \mathcal{A}_{\mathbf{m}, \mathbf{n}} + \left(\left[\tilde{\Delta}_{\mathbf{m}, \mathbf{n}}^{\mu, \nu} + \beta_{\mu, \nu} D_{\mathbf{m}, \mathbf{n}} \right] \tau_- + \text{h.c.} \right) + \mathcal{V}_{\mathbf{m}, \mathbf{n}}, \quad (\text{S.38})$$

where $H_{\mathbf{m}, \mathbf{n}}^{\mu, \nu} = \langle \mu, \mathbf{m} | H | \nu, \mathbf{n} \rangle$ and $\mathbf{n} = (n_x, n_y)$. Here, the various matrix elements are given by

$$\varepsilon_{\nu, \mathbf{n}} = \varepsilon_\nu + \hbar\omega_t (n_x + n_y), \quad (\text{S.39})$$

$$k_z^{\mu, \nu} = \langle \varphi_\mu | \hat{k}_z | \varphi_\nu \rangle \in i\mathbb{R}, \quad (\text{S.40})$$

$$\mathcal{A}_{\mathbf{m}, \mathbf{n}} = \frac{\hbar^2 \pi}{m_l \Phi_0} \langle \chi_{\mathbf{m}} | A_z | \chi_{\mathbf{n}} \rangle = \frac{\hbar^2 \pi}{m_l \Phi_0} (B_x y^{\mathbf{m}, \mathbf{n}} - B_y x^{\mathbf{m}, \mathbf{n}}) \in \mathbb{R}, \quad (\text{S.41})$$

$$\tilde{\Delta}_{\mathbf{m}, \mathbf{n}}^{\mu, \nu} = \langle \varphi_\mu \chi_{\mathbf{m}} | V e^{-i2k_0 z} | \varphi_\nu \chi_{\mathbf{n}} \rangle \in \mathbb{C}, \quad (\text{S.42})$$

$$\beta_{\mu, \nu} = \beta_0 \langle \varphi_\mu | e^{i2k_1 z} | \varphi_\nu \rangle \in \mathbb{C}, \quad (\text{S.43})$$

$$D_{\mathbf{m}, \mathbf{n}} = k_x^{\mathbf{m}, \mathbf{n}} \sigma_x - k_y^{\mathbf{m}, \mathbf{n}} \sigma_y, \quad (\text{S.44})$$

$$\mathcal{V}_{\mathbf{m}, \mathbf{n}}^{\mu, \nu} = \langle \varphi_\mu \chi_{\mathbf{m}} | V_{\text{dis}} | \varphi_\nu \chi_{\mathbf{n}} \rangle \in \mathbb{R}, \quad (\text{S.45})$$

where

$$x^{\mathbf{m}, \mathbf{n}} = \delta_{m_y, n_y} \frac{\ell_t}{\sqrt{2}} (\sqrt{m_x} \delta_{m_x, n_x+1} + \sqrt{n_x} \delta_{m_x, n_x-1}) \in \mathbb{R}, \quad (\text{S.46})$$

$$y^{\mathbf{m}, \mathbf{n}} = \delta_{m_x, n_x} \frac{\ell_t}{\sqrt{2}} (\sqrt{m_y} \delta_{m_y, n_y+1} + \sqrt{n_y} \delta_{m_y, n_y-1}) \in \mathbb{R}, \quad (\text{S.47})$$

$$k_x^{\mathbf{m}, \mathbf{n}} = \delta_{m_y, n_y} \frac{i}{\sqrt{2} \ell_t} (\sqrt{m_x} \delta_{m_x, n_x+1} - \sqrt{n_x} \delta_{m_x, n_x-1}) \in i\mathbb{R}, \quad (\text{S.48})$$

$$k_y^{\mathbf{m}, \mathbf{n}} = \delta_{m_x, n_x} \frac{i}{\sqrt{2} \ell_t} (\sqrt{m_y} \delta_{m_y, n_y+1} - \sqrt{n_y} \delta_{m_y, n_y-1}) \in i\mathbb{R}, \quad (\text{S.49})$$

and $\ell_t = \sqrt{\hbar/(m_t \omega_t)}$ is the characteristic dot size in the transverse direction.

To obtain the effective Hamiltonian Eq. (3) in the main text, we perform a second-order Schrieffer-Wolff transformation of Eq. (S.38), treating all the excited orbital states $\nu, \mathbf{n} > 0$ as perturbations. In this way, the inter-valley coupling is given by [29]

$$\Delta = \tilde{\Delta}_{\mathbf{0}, \mathbf{0}}^{0,0} - 2 \sum'_{\nu, \mathbf{n}} \frac{\mathcal{V}_{\mathbf{0}, \mathbf{n}}^{0, \nu} \tilde{\Delta}_{\mathbf{n}, \mathbf{0}}^{\nu, 0}}{\varepsilon_{\nu, \mathbf{n}} - \varepsilon_0}, \quad (\text{S.50})$$

where the prime notation indicates that the ground state is not included in the sum. The spin-orbit coupling term is given by

$$g_\tau = \frac{2e\hbar}{\mu_B m_l} \sum_{\nu > 0} \frac{(ik_z^{0,\nu})\beta_{\nu,0}}{\varepsilon_\nu - \varepsilon_0 + \hbar\omega_t}, \quad (\text{S.51})$$

which involves momentum and spin-orbit matrix elements defined in Eqs. (S.40) and (S.43). We note that, at this level of approximation, Δ includes correction terms arising from the alloy-disorder matrix elements \mathcal{V} and $\tilde{\Delta}$, which couple the lowest-energy orbital to higher-energy orbitals, while g_τ does not. To compute these disorder terms, we make use of their statistical description, given by a multivariate normal distribution whose covariance elements are derived in the Supplementary Materials of Ref. [29]. Alloy disorder is therefore included by calculating the relevant covariance elements and sampling the resulting multivariate normal distributions.

To calculate the g -factor numerically, as in necessary for generating the data in Fig. 2(g) of the main text, we project Eq. (S.38) onto a finite basis set and solve for the two lowest-energy eigenstates in the limit of $B \rightarrow 0$. We check for convergence by increasing the number of subbands and harmonic oscillator orbitals included in the basis set.

S.6. EXPLANATION FOR WHY HIGHER-ORDER ALLOY-DISORDER INDUCED FLUCTUATIONS IN g ARE SMALL

In the main text, we noted that some higher-order alloy-disorder terms were not included in the effective Hamiltonian of Eq. (3), although in principle, they could interfere with our ability to invert g to obtain the valley phase ϕ_v . In Fig. 2(g), we showed that such corrections to g are very small by collecting statistics on the valley-phase error $|\phi_v^{(g)}| - |\phi_v|$. Here, we provide two arguments for why the disorder-induced corrections are small.

First, the corrections to g_τ involving disorder enter only at third-order in the perturbation theory, while second-order corrections are all deterministic. Compared to second-order terms, the disorder-induced terms are suppressed by the ratio of the disorder energy scale (tens of μeV) to the subband energy splitting (tens of meV), which is very small. Second, the deterministic contributions to g_τ are seen to be relatively large compared to the deterministic contributions to Δ_0 . This is because the spin-orbit matrix element $\beta_{\mu,\nu}$ in Eq. (S.43) requires “sharp” features in the quantum well, of length scale $\pi/k_1 \approx 1.6$ nm, which are fairly easy to engineer in modern devices. This should be compared to the inter-valley coupling term $\tilde{\Delta}_{\mathbf{m},\mathbf{n}}^{\mu,\nu}$ in Eq. (S.42) that requires sharp features of length scale $\pi/k_0 \approx 0.32$ nm, which are much more difficult to achieve in experiments, as noted in several previous works [13–16]. It is therefore reasonable that Δ is typically dominated by disorder effects, while g_τ is most strongly affected by deterministic effects.